A Thermal Fluid-Dynamic Steady State Analysis of the EADF Downcomer Channel

C. Aragonese, S. Buono, G. Fotia, L. Maciocco, V. Moreau, L. Sorrentino

Cagliari, April 4, 2000

Abstract

In this work a numerical simulation of the Energy Amplifier Demonstration Facility (EADF) [1, 2] downcomer channel is presented. The simulation is fully three-dimensional (3D) and is focused on a Steady-State Analysis. All relevant heat transfer phenomena are taken into account.

The Intermediate Heat eXchangers (IHX) of the EADF reference configuration are immersed in the lead-bismuth eutectic of the downcomer and no physical barrier separates the hot and cold collectors.

As expected, the simulation shows a thermal stratification outside the IHX, whose characteristics mainly depend on the IHX pressure loss. A parametric study of the effects of the IHX pressure loss coefficient on the thermal stratification pattern is presented.

1 Introduction

In this work a numerical simulation of the Energy Amplifier Demonstration Facility (EADF) [1, 2] downcomer channel and its interaction with the Intermediate Heat eXchangers (IHX) is presented. The simulation is fully three-dimensional (3D) and is focused on a Steady-State Analysis. Both the primary and secondary fluids are simulated in the IHX and all relevant heat transfer phenomena are taken into account.

A one-dimensional simulation of the overall circuit can be found in [3], and a one-dimensional simulation of the downcomer channel can be found in [4]. Other studies have been done on other specific parts of the system [5, 6]. Here we are interested in the flow circulation of the primary coolant in the downcomer of the primary circuit. A first analysis on a simplified 3D geometry has already been done in [7] and is continued in the present paper which focuses on the thermal fluid-dynamic parametric analysis for steady state flow configurations, the parameter being the IHX pressure loss.

The IHXs of the EADF reference configuration are immersed in the lead-bismuth eutectic of the downcomer. Because there is no physical barrier separating the hot and cold collectors, the percentage of the coolant flowrate that flows inside the IHX depends on the weight difference between the cooled fluid inside the the IHX and the hot fluid beside it and, precisely, it is determined by the equilibrium between the above weight difference (driving force) and the pressure loss through the IHX.

Besides the IHX performance, an important aspect of the thermal-hydraulic design of the downcomer subsystem, is that the thermal stresses have to be kept as low as possible, avoiding strong thermal gradients in the critical parts of the structure. The position and intensity of such gradients is evidentiated by the numerical simulation.

2 Geometric Description

The global geometric description of the EADF downcomer channel and its cross-section structure are shown in figures 1 and 2.

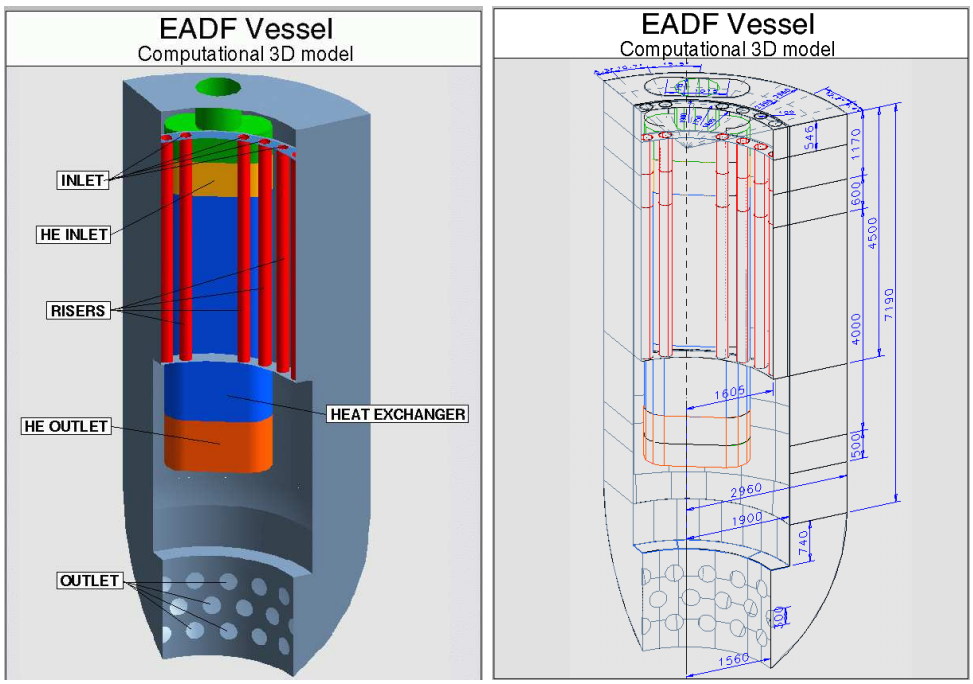

Figure 1: One quarter of the EADF downcomer channel. Distances are in millimeters.

Only a quarter of the full domain is drawn for symmetry reasons (see section 5.1). The Pb-Bi eutectic enters the domain rising inside the vertical red pipes and

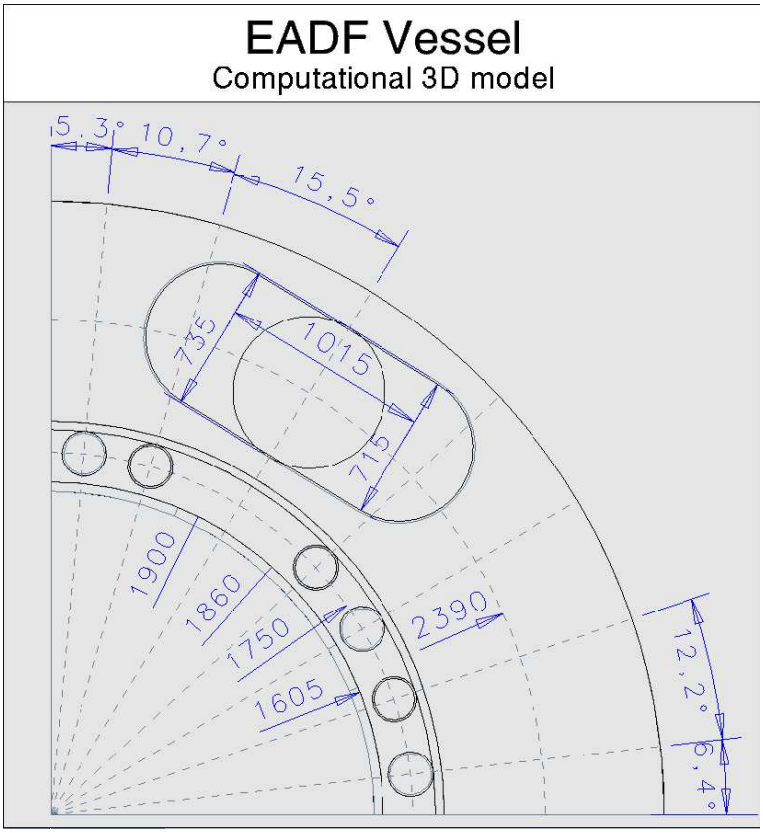

Figure 2: Geometrical structure of an horizontal section of the EADF Vessel.

leaves the domain at the bottom part through a drilled shell to turn back to the core. The yellow and blue parts represent the IHX. The yellow part is unshielded and the flow enters at this level. The blue part is shielded and the orange part is just the shell guiding the flow vertically under the IHX (skirt). The green part is the secondary coolant feeding tube.The upper shell of the domain simulates the free surface.

3 General Parameters

3.1 Global Parameters

The global parameters of the primary circuit are reported below. The values of the extensive parameters are reported both for the whole vessel and for the quarter of the vessel effectively simulated.

Coolant: Lead-Bismuth Eutectic[1]

Nominal power: $Pw = 4 \times 20.75 = 83\ MW$

Mass flow rate: $\dot{M} = 4 \times 1449 = 5.8 \cdot 10^3\ kg\, s^{-1}$

Volume flow rate: $\Phi_{inlet} = 4 \times 0.142 = 0.57\ m^3\, s^{-1}$

Inlet and reference temperature $T_{inlet} = T_{ref} = 673\ K = 400\ ^oC$

Resulting temperature difference: $\Delta T = 100\ K$

Volume of coolant: $Vol_c = 4 \times 37.5 = 150\ m^3$

3.2 Coolant properties

The values reported below are taken from [8]. Reference values corresponding to the inlet temperature are also reported.

Density: $\rho = 10186\ kg\, m^{-3}$ at $T_{in} = 400\ ^oC$

$$\rho = \begin{cases} 11112 - 1.375T & \text{(T in } K) \\ 10737 - 1.375T & \text{(T in } ^oC) \end{cases} \tag{1}$$

[1]The Lead is 44.5% of the weight.

Laminar viscosity: $\mu = 1.50 \cdot 10^{-3}\ kg\, m^{-1}\, s^{-1}$ at $T_{in} = 400\ ^oC$

$$\mu = \begin{cases} 4.71 \cdot 10^{-9} T^2 - 8.92 \cdot 10^{-6} T + 5.37 \cdot 10^{-3} & \text{(T in } K) \\ 4.63 \cdot 10^{-9} T^2 - 6.26 \cdot 10^{-6} T + 3.26 \cdot 10^{-3} & \text{(T in } ^oC) \end{cases} \tag{2}$$

Specific heat: $Cp = 146.5\ J\, kg^{-1}\, K^{-1}$

Thermal conductivity: $k = 12.2\ W\, m^{-1}\, K^{-1}$ at $T_{in} = 400\ ^oC$

$$k = \begin{cases} 3.90 + 0.0123T & \text{(T in } K) \\ 7.26 + 0.0123T & \text{(T in } ^oC) \end{cases} \tag{3}$$

Melting point: $T_M = 398\ K = 125\ ^oC$

Boiling point: $T_B = 1912\ K = 1639\ ^oC$ at $101,325\ Pa$.

4 IHX main geometrical characteristics

The IHXs are of the bayonet type [2] and are immersed in the primary coolant (Pb-Bi) without any solid structure separating the hot and cold collectors in the region around the IHXs.

The IHX is enclosed in a 2cm steel shell, except for the upper 60 cm which serve as inlet region. The skirt goes 90cm deeper than the tubes to enhance the pumping effect. The characteristics relevant for the numerical simulation are given below:

Volume: $Vol_{ihx} = 5.36\ m^3$

Superficial area: $A = 1.16\ m^2$

Height: $H = 4.6\ m$

Heat exchange surface: $S_{ihx} = 425\ m^2$

Number of tubes: $N_{tu} = 1364$

Tubes thickness: $\delta r = 1.2446 \cdot 10^{-3}\ m$

Tubes external radius: $R_{tu} = 11.112\ mm$

Perimeter: $Per = 4.34\ m$

Porosity: $Por = \frac{1}{A} \cdot (A - N_{tu} \pi R_{tu}^2) = 0.544$

Hydraulic diameter: $D = \frac{4A \cdot Por}{Per + N_{tu}.2\pi R_{tu}} = 0.0249\ m$

The following parameters are defined:

Reynolds number[2] : $Re_{ihx} = \frac{\rho \bar{v}_{ihx} \cdot D}{\mu}$

Pressure drop coefficient [3]: $f = 0.079 Re_{ihx}^{-0.25}$

Distributed pressure drop [4]: $\Delta P_r = \frac{2\rho f H \bar{v}_{ihx}^2}{D}$

5 Numerical implementation

5.1 Symmetry

From purely geometrical considerations, we should have simulated at least half of the physical domain, as can be seen in figure 3. Nevertheless, we have simulated only one quarter of the domain which allows a correct description of the inlet flow distribution. This approximation is expected to be irrelevant while the gain in computational resources is critical. A symmetry boundary condition has been imposed on the cutting sections.

5.2 Free Surface

The free surface at the top of the coolant is not simulated. We just put a rigid horizontal wall in correspondence of the mean surface level that the fluid is expected to reach under nominal operating condition. The simulation of the free surface is quite expensive from the computational point of view and its reliability is not clearly established. Moreover, the inlet flow should be a bubbly flow, with the bubbles escaping through the free surface. The combined effect on the flow of the presence of the bubbles, the free surface and their interaction is not known and should be the object of future studies. Anyway, the effect of the presence of the free surface is expected to be localized to the upper part of the domain and have a minimum influence on the thermal-hydraulic field in the rest of the domain.

5.3 Inlet

5.3.1 Geometrical considerations

The inlet consists of 24 holes corresponding to the outlet of the 24 rising pipes of $r_{pipe} = 0.1\ m$ internal radius for a total inlet area of $A_{inlet} = 24\pi r_{pipe}^2 = 4 \times 0.1885 =$

[3] Based on a relative roughness close to 0.0008 and a Reynolds number close to 40000, according to [9].

[4] Darcy's formula

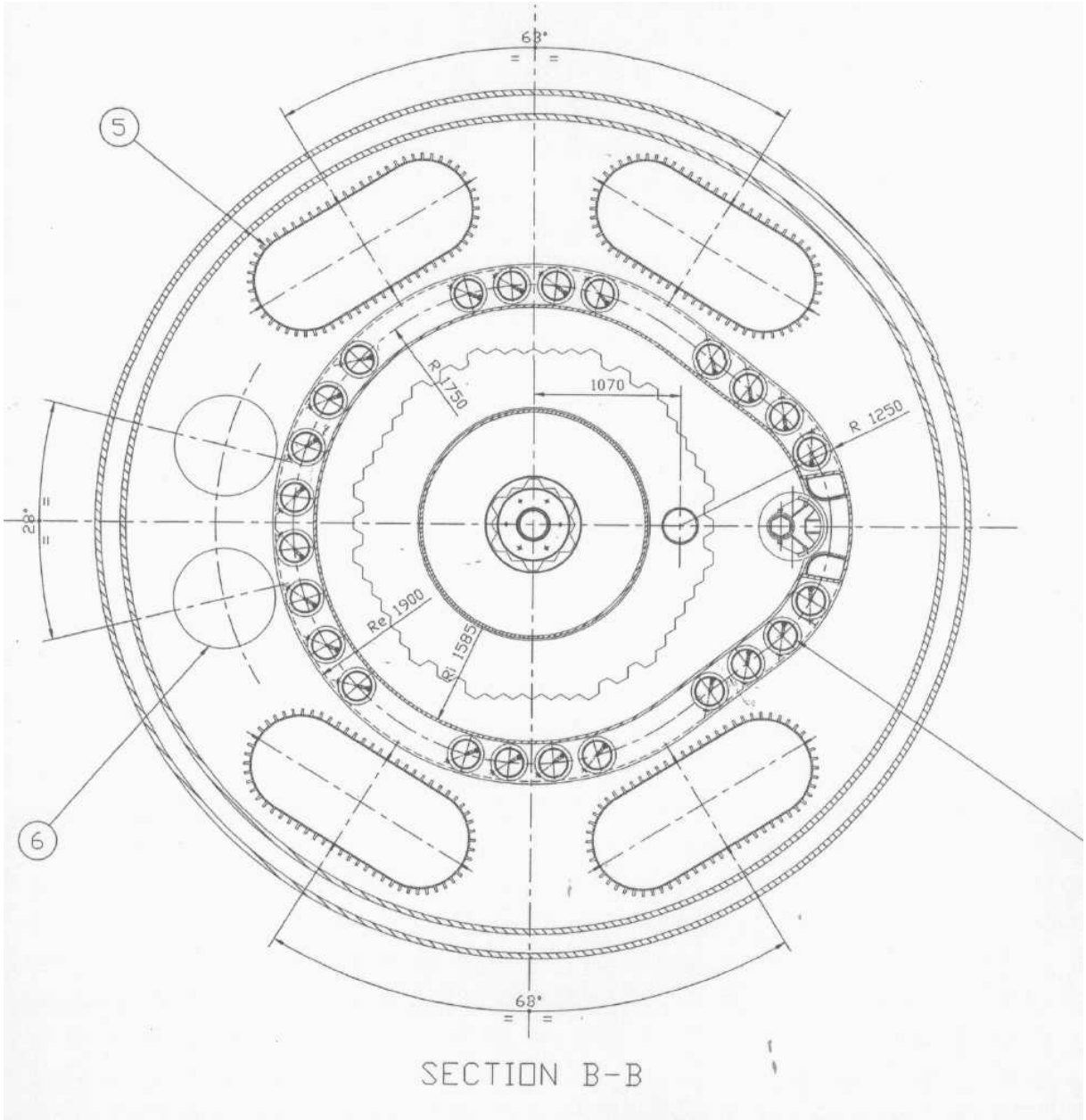

Figure 3: Horizontal sketch of the EADF vessel with the 4 IHX and the 24 rising tubes.

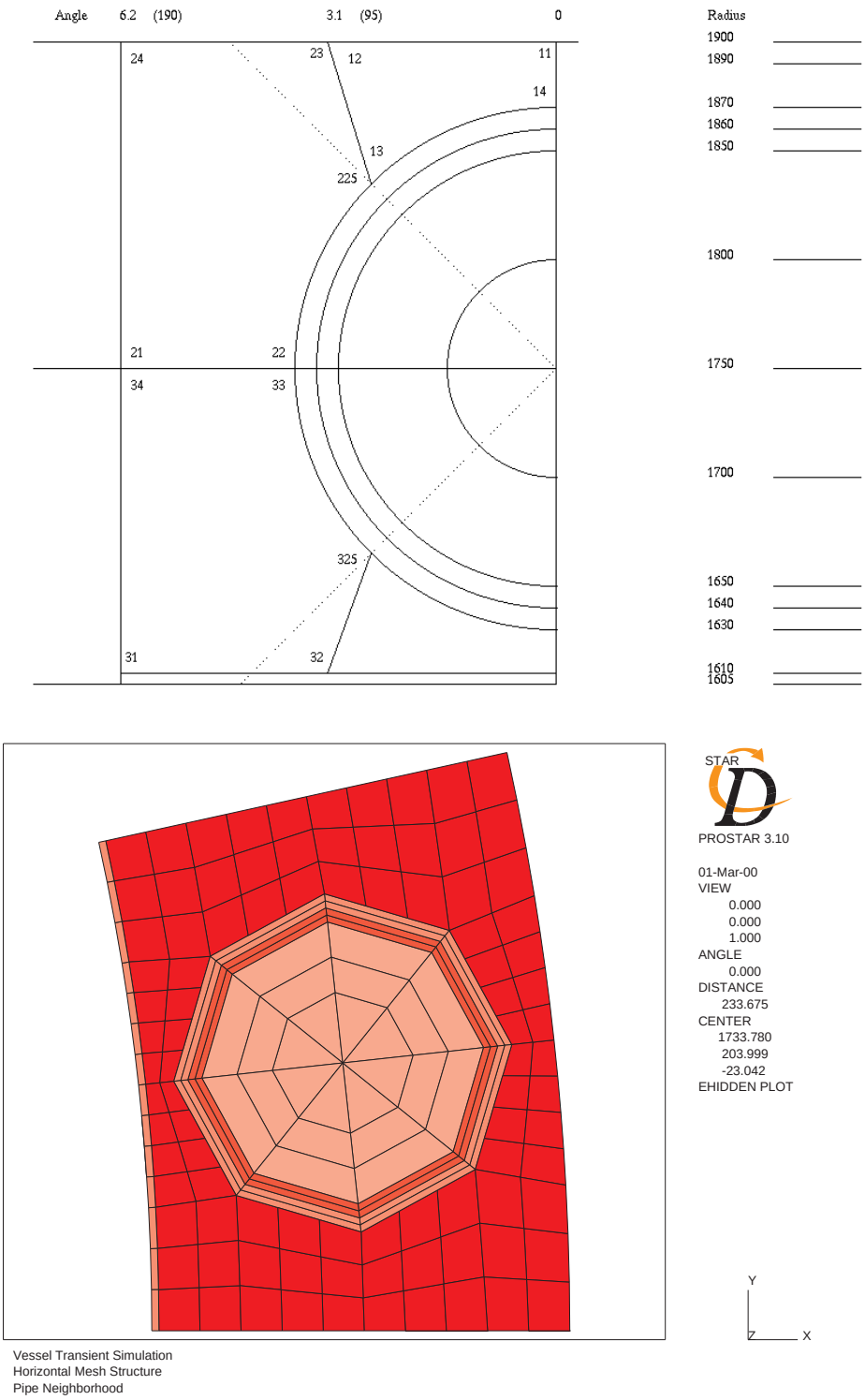

Figure 4: Top: topological structure on half pipe. Bottom: resulting mesh for a full pipe.

$0.7540\ m^2$. There are six inlet pipes in the computational domain. Previous simulations [7] have shown that the geometrical description of the pipes should not be excessively rough. A special effort has been made to describe all pipes to a relative high level of accuracy. The pipes section is approximated with an octagon inscribed in the real circular perimeter. The pipes interior is not simulated but their upper (octagonal) extremity is decomposed in 24 plane triangular cells for the inflow description. A description of the mesh in the pipes region is shown in figure 4 along with its topological structure.

5.3.2 Mass flow rate

The inlet mass flow rate is calculated in order to satisfy the relation

$$\dot{M} C_p \Delta T = P_w \tag{4}$$

with a small correction to take into account the global heat transfer balance through the walls. The local mass flow rate must be carefully preserved at the inlet. There is a small discrepancy between the surface of a circle (πr^2) and the surface of the inscribed octagon ($2\sqrt{2}r^2$), which is close to 10%. The pipes have an internal radius of $r_{pipe} = 10\ cm$. This leads to an effective numerical inlet surface and inlet fluid velocity of:

$$A_{inlet} = 24 \times 2\sqrt{2} r_{pipe}^2 = 0.679\ m^2, \tag{5}$$

$$v_{inlet} = \Phi_{inlet}/A_{inlet} = 0.838\ m\,s^{-1}. \tag{6}$$

This velocity is a little higher than the expected mean velocity in the pipes which would be for a true circular configuration:

$$v_\pi = 0.754\ m\,s^{-1}, \tag{7}$$

but is consistent with a bubbly flow with a void fraction of about 10%.

5.3.3 Turbulent parameters

The inlet turbulent intensity $\mathcal{I}_{inlet}$ and the turbulent length scale l_{inlet} must be specified when applying the $k-\varepsilon$ turbulent model. We assigned $l_{inlet} = 0.2\ m$ equal to the diameter of the inlet tubes and $\mathcal{I}_{inlet} = 0.01$. This last value has no real justification but it has little relevance for this flow configuration.

5.4 Outlet

In [7], we simulated only the cylindrical part of the vessel down to the level $-6920\ mm$. Unfortunately the simulation result gave inflow through the outlet. So we added the bottom region, simulating the outlet holes as one single centered rectangular big outlet of the same total area to simplify the mesh modelling.

5.5 Heat exchanger

5.5.1 Momentum equation

A detailed simulation of the IHX would have prohibitive computational costs. Therefore, it is simulated as a porous media. The Darcy's formula is used to calculate a local momentum source equivalent to the theoretical pressure loss. The local implementation of the Darcy's formula in term of the the global hydraulic diameter is acceptable because the cell scale hydraulic diameter is nearly equal to the global hydraulic diameter. The resulting vertical momentum source term $\dot{S}_w$ is given by

$$\dot{S}_w = -C_1 \cdot |w_s|^{0.75} \cdot w_s \tag{8}$$

with

$$C_1 = -\frac{0.079 \cdot 2 \cdot \mu^{0.25} \cdot \rho^{0.75}}{D^{1.25} \cdot Por^{1.75}} \tag{9}$$

where w_s is the superficial vertical velocity, namely $w_s = Por \cdot w$ where w is the real vertical velocity. Note that this expression is valid only for a given range of Reynolds number, and should scale like w_s at very low Re_{ihx} and like w_s^2 at very high Re_{ihx}.

The value of C_1 is fixed by taking the physical parameters at $350\ ^oC$:

$$C_1 = 1.0024 \cdot 10^4\ kg\, m^{-3.75}\, s^{-0.25} \tag{10}$$

The treatment of the non-linearity in w_s can be done by mean of a user-subroutine or using a direct feature of the software allowing for a linear plus quadratic approximation of $\dot{S}_w$:

$$\dot{S}_w = -C_2 \cdot w_s - C_3 \cdot w_s^2. \tag{11}$$

Note that, according to [10] (chapter 8), C_2 should be strictly positive in presence of a stagnation point, as it is the case on top of the IHX, for numerical stability reasons. For the same reasons, a direct implementation through user-subroutine should introduce a cut-off value under which $\dot{S}_w$ is linear in w_s.

We take the simpliest choice of taking $\dot{S}_w$ linear in w_s, that is $C_3 = 0$. Clearly, a more elaborated treatment must be done to capture accurately transient situations. The remaining part, namely $|w_s|^{0.75}$ is approximated with the assumption that all the flow passes through the IHX, namely,

$$|w_s| \simeq \frac{\Phi_{inlet}}{A} \tag{12}$$

which leads to

$$C_2 = 2075\ kg\, m^{-3}\ s^{-1} \tag{13}$$

By the way, this value is only indicative, being the length and arrangement of the IHX tubes subject to variations.

The IHX inlet is lateral and 60 cm high, so it is not trivial to define the IHX length if one wants to calculate, say, the pressure drop through the IHX using a 1D correlation. Anyway, we need to define in a consistant way the global friction pressure drop ΔP_f and the global buoyancy pressure gain ΔP_b for the IHX.

Our approach is based on the calculation of global work of friction and buoyancy forces scaled by the volume flow rates.

We call $\dot{W}_f$ the work of the friction force, $\vec{\dot{S}} = (\dot{S}_u, \dot{S}_v, \dot{S}_w)^T$, per unit time:

$$\dot{W}_f = \int_{IHX} \vec{\dot{S}} \cdot \vec{v_s}. \tag{14}$$

We call

$$\vec{F_b} = -\beta(T - T_{ref}) \cdot \vec{g} \tag{15}$$

the buoyancy force, where T_{ref} is the reference temperature ($T_{ref} = 400\ ^oC$).

We call $\dot{W}_{b,in}$ and $\dot{W}_{b,out}$ the work of the buoyancy force per unit time inside the IHX and outside the IHX:

$$\dot{W}_{b,in} = \int_{IHX} \vec{F_b} \cdot \vec{v_s} \tag{16}$$

$$\dot{W}_{b,out} = \int_{IHXoutside} \vec{F_b} \cdot \vec{v}. \tag{17}$$

We define the friction pressure drop ΔP_f to be:

$$\Delta P_f = \frac{\rho \dot{W}_f}{\dot{M}_{ihx}} \tag{18}$$

and we define the buoyancy pressure gain ΔP_b to be:

$$\Delta P_b = \frac{\rho \dot{W}_{b,in}}{\dot{M}_{ihx}} - \frac{\rho \dot{W}_{b,out}}{\dot{M} - \dot{M}_{ihx}}. \tag{19}$$

When the flow outside the IHX vanishes the second term of the right-hand-side in the former equation becomes undefined and we replace equations (15) and (19) with the following:

$$\vec{\tilde{F}_b} = -\beta(T - \bar{T}_{out}(z)) \cdot \vec{g} \tag{20}$$

$$\Delta P_b = \frac{\rho}{\dot{M}_{ihx}} \int_{IHXinside} \vec{\tilde{F}_b} \cdot \vec{v_s} \tag{21}$$

where $\bar{T}_{out}(z)$ is the average temperature outside the IHX over the plane of level z.

The quantities ΔP_b and ΔP_f can be calculated in post-processing and will be given in the results section.

The friction factor ξ used in reference [4] (pressure loss $\Delta P_f = \xi \cdot \frac{w^2}{2} \cdot \rho$) is obtained from ΔP_f by the formula:

$$\xi = \frac{2\rho \cdot Por^2 \cdot A^2}{\dot{M}_{ihx}^2} \cdot \Delta P_f \tag{22}$$

having used $w = \frac{\dot{M}_{ihx}}{\rho \cdot A}$, where $\dot{M}_{ihx}$ is he actual mass flow rate through the IHX. When it is equal to the total mass flow rate $\dot{M}$, then we have, for a porosity of 0.5:

$$\xi = 3.28 \cdot 10^{-3} \cdot \Delta P_f. \tag{23}$$

5.5.2 Enthalpy equation

The model for the simulation of the heat exchanges inside the IHX has been considerably improved compared to the previous work [7]. Both the primary and the secondary coolant are simulated. The IHX region is modelled as a group of three porous media occupying the same physical space. The first one is dedicated to the primary coolant and has already been described. The two others are dedicated to the secondary coolant, one for the descending flow and one for the ascending flow. The heat transfer is simulated by adding a source term $\dot{H}_{he}$ in the enthalpy equation which is proportional to the temperature difference at the same position between pairs of cells in the porous media. The primary coolant and the descending secondary coolant exchange heat with the ascending flow region. The heat transfer is also proportional to the density of exchange surface (S_{he}/Vol_{he}) and to the IHX global heat transfer coefficient. The overall heat exchange coefficients are assumed constant and their value, calculated in [4, 11], are:

$$G_p = 1.1586 \cdot 10^5 \; W\,K^{-1}\,m^{-3} \qquad \text{primary-secondary coolant} \tag{24}$$

$$G_s = 0.5228 \cdot 10^5 \; W\,K^{-1}\,m^{-3} \qquad \text{rising-downcoming secondary coolant.} \tag{25}$$

5.6 Heat transfer accross solid walls

Apart from the primary-secondary coolant heat transfer, many other heat exchanges have been taken into account accross solid walls in the computational domain. On a case-by-case basis, we have used specific features of the code. In the following, we give a description of the heat transfer implementation. The walls location is shown on a radial profile of the downcomer channel in figure 5. The capital letters given below refer to the capital letters in this figure.

- **Heat flux**: the EADF can release heat through a safety device called RVACS, which is external to the vessel and is based on the natural convection of external (ambient) air. The heat flux (ψ) depends on the Vessel outer wall temperature (T_w, expressed in ^oC) according to the following law[12]:

$$\psi = -158. + 1.57 \cdot T_w - 1.52 \cdot 10^{-2} \cdot T_w^2 \text{ in } W\,m^{-2}. \tag{26}$$

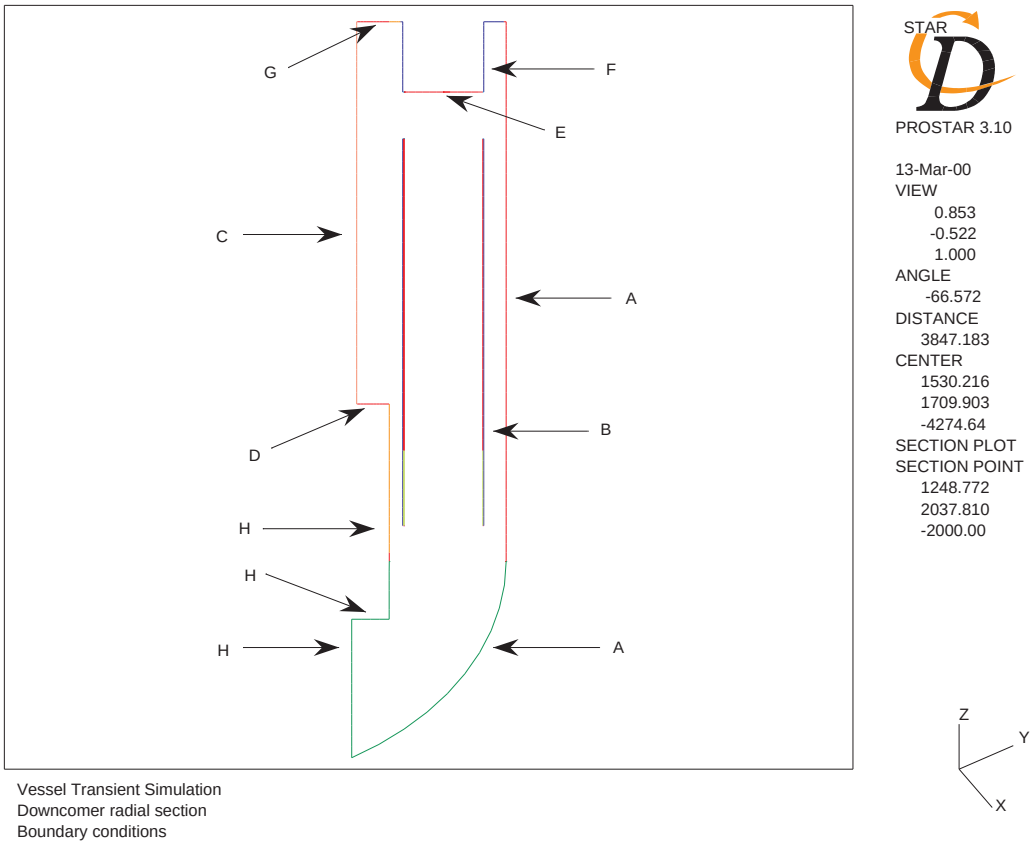

Figure 5: Solid walls of the downcomer channel: (A) outer wall, (B) IHX shell, (C) inner wall behind the tubes, (D) rising tubes support, (E) bottom of IHX feeding tube connection, (F) lateral of IHX feeding tube connection, (G) cover wall, (H) inner walls under the pipes.

Material	Pb-Bi	oil	solid	total
Number of cells	142,318	29,040	11,200	182,558

Table 1: Number of cells used for the numerical simulation for each material and for the whole domain.

This law is used to set the local heat flux on the vessel outer wall (A).

- **Conducting Walls**: the IHX shell (B) is actually meshed and conjugate heat transfer is calculated on these solid cells.
- **Fixed temperature walls**: heat fluxes through the walls listed below are simulated by setting a fixed temperature with a given resistance corresponding to the wall characteristics (conductivity and width):
  - Tube walls: fixed temperature at $400\ ^oC$ with resistance $h = 5.5{\cdot}10^{-5}\ m^2\,K\,W^{-1}$.
  - Wall behind the tubes (C): fixed temperature at $400\ ^oC$ with resistance $h = 2. \cdot 10^{-3}\ m^2\,K\,W^{-1}$.
  - Rising tubes support (D): fixed temperature at $400\ ^oC$ with resistance $h = 1. \cdot 10^{-3}\ m^2\,K\,W^{-1}$.
  - Bottom of IHX feeding tube connection (E): fixed temperature at $320\ ^oC$ with resistance $h = 6. \cdot 10^{-3}\ m^2\,K\,W^{-1}$.
  - Lateral and top of IHX feeding tube connection (F): fixed temperature at $320\ ^oC$ with resistance $h = 1.5 \cdot 10^{-3}\ m^2\,K\,W^{-1}$.
- **Adiabatic Walls** The cover wall (G) and the inner walls under the pipes (H), separating the downcomer from the core region, are treated as adiabatic.

5.7 Mesh structure

The domain has been meshed following a block-structured strategy. The first $6.92m$ ($4.5m$ for the inlet tubes) are constructed by extruding the planar 2D-mesh shown in figure 6 while the bottom part is just one structured 3D-block. The connection to the upper part is non-matching. The number of cells used for the numerical simulation for each material and for the whole domain is shown in table 1.

6 Results and discussion

We present here six simulations differing only by the set up of the pressure losses in the IHX.

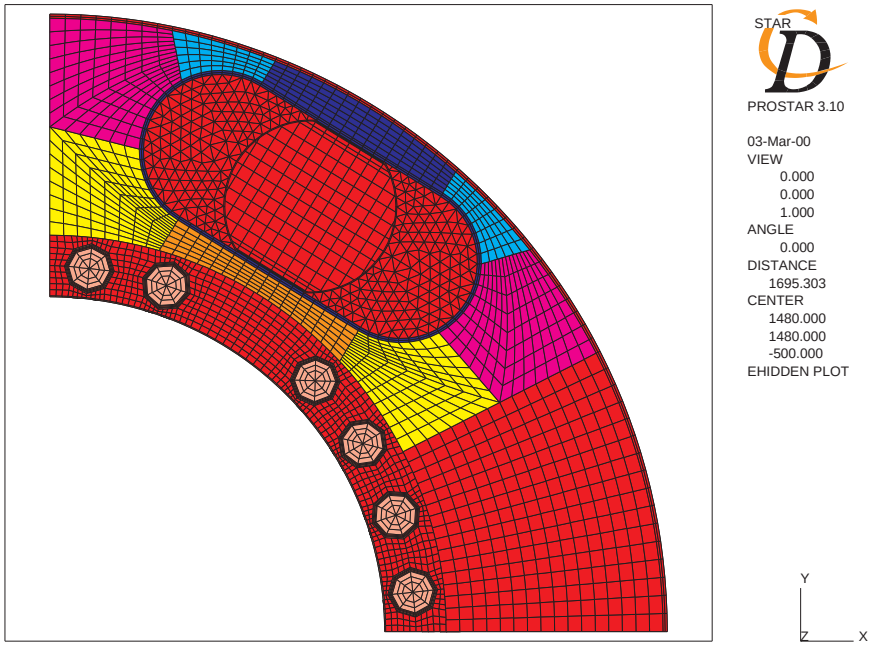

Vessel Transient Simulation
Mesh Structure
Top View

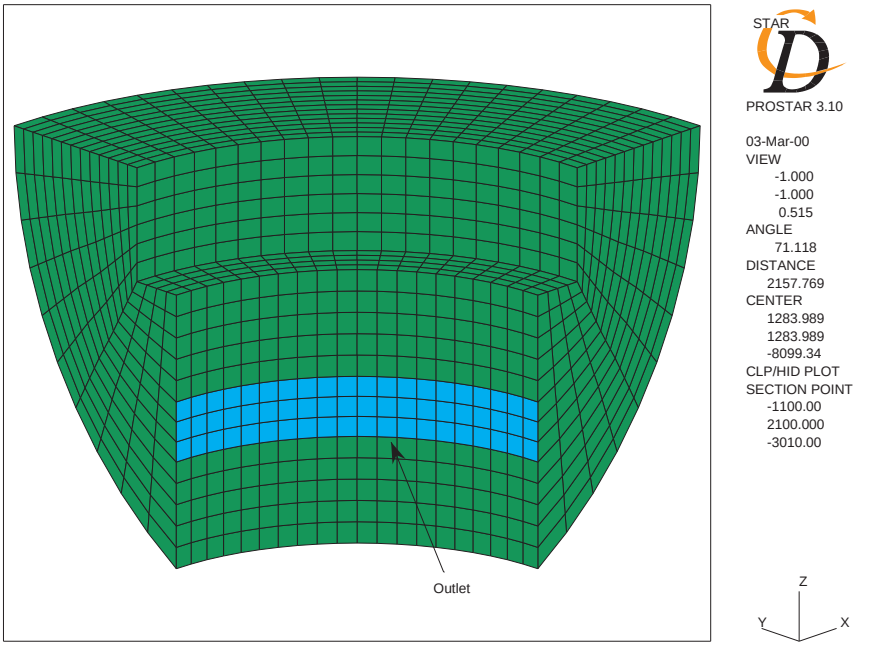

Vessel Transient Simulation
Mesh Structure
Bottom Part with Outlet highlighted

Figure 6: One quarter of the EADF. Mesh structure of an horizontal section and bottom mesh with outlet localization.

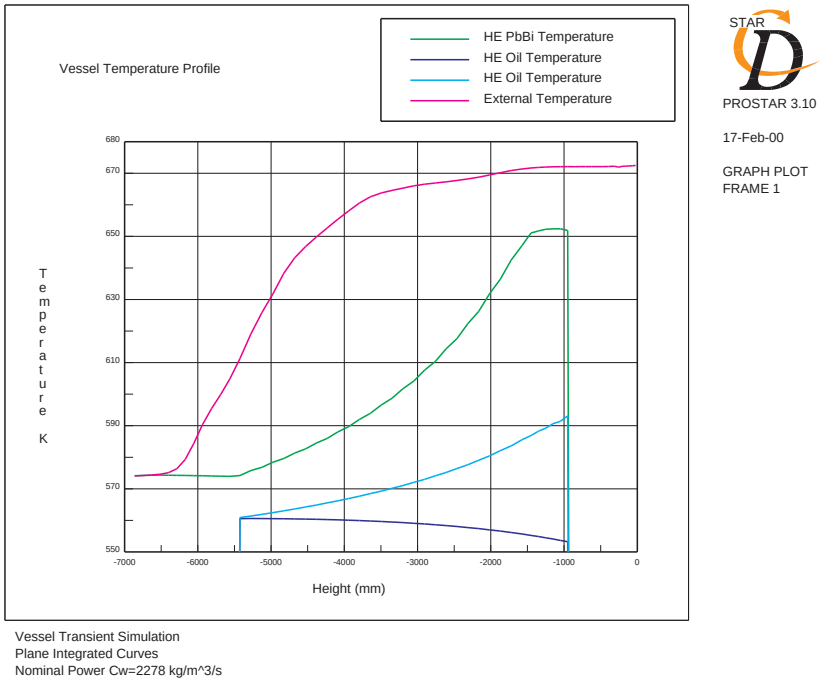

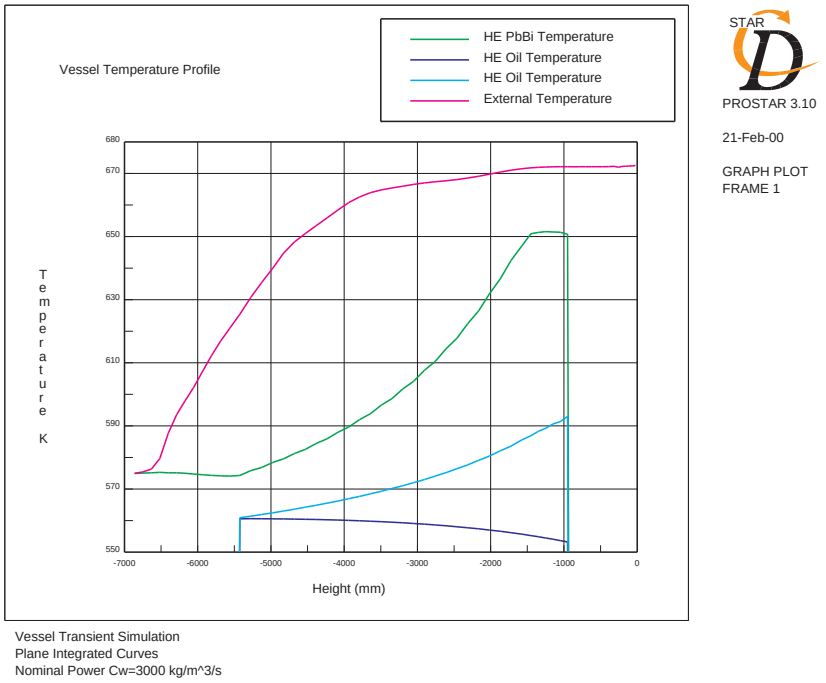

Figure 7: Mean temperature profiles along the vertical axis for case 1 (up) and case 2 (down).

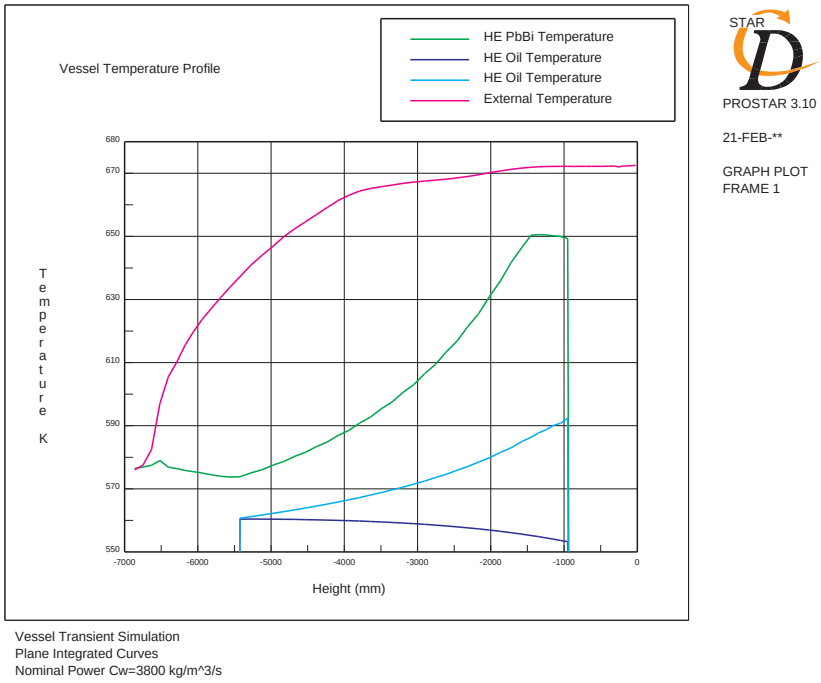

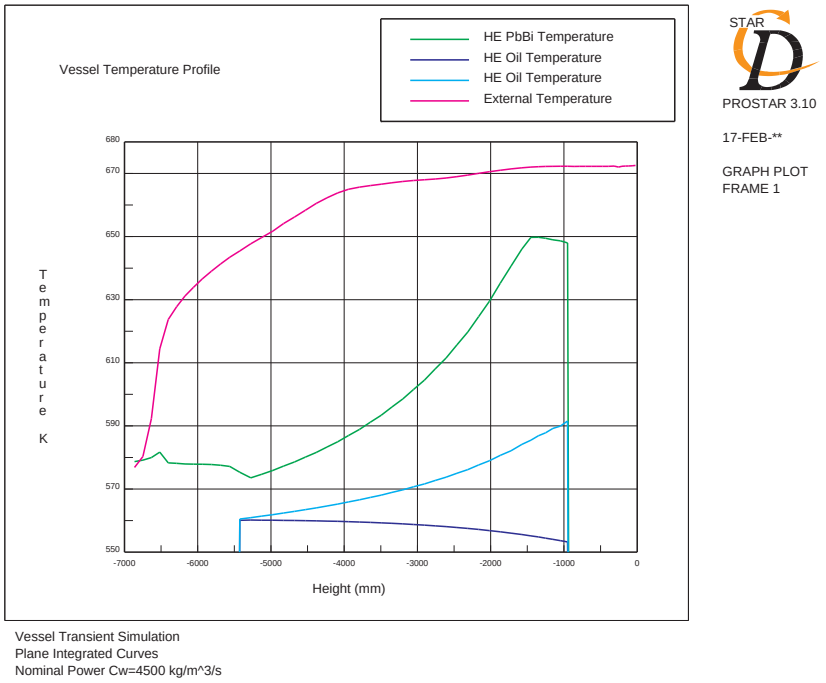

Figure 8: Mean temperature profiles along the vertical axis for case 3 (up) and case 4 (down).

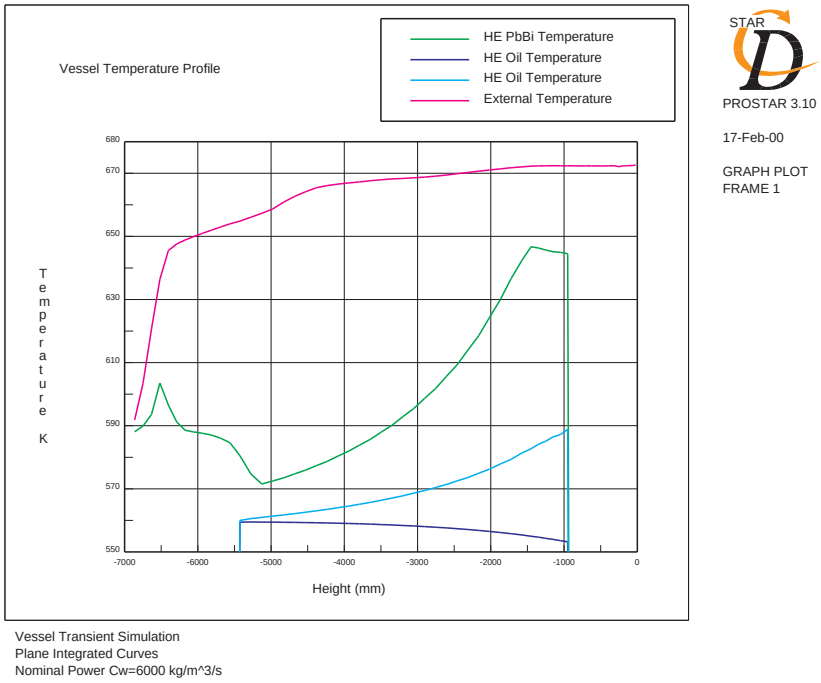

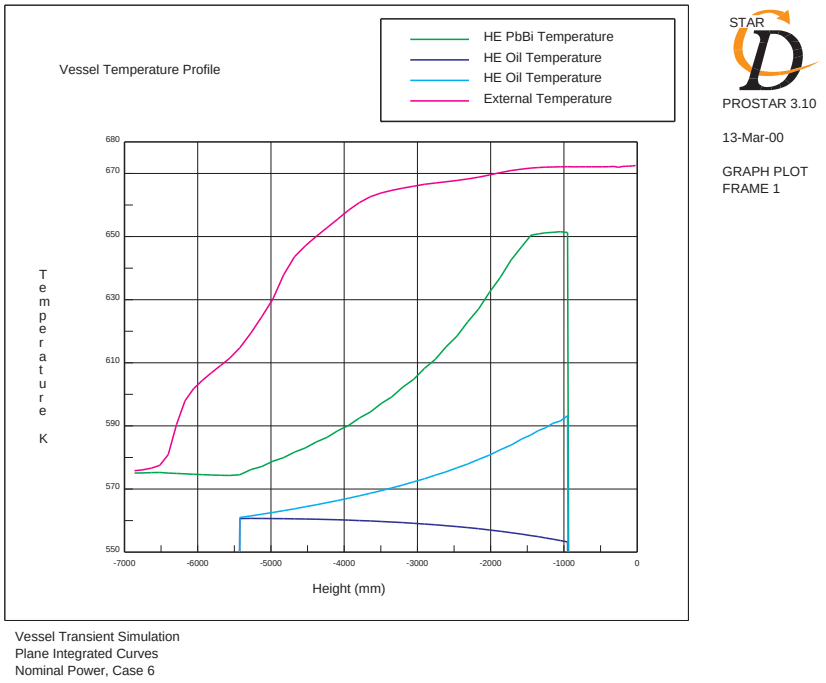

Figure 9: Mean temperature profiles along the vertical axis for case 5 (up) and case 6 (down).

Case	1	2	3	4	5	6
$\Delta P_f(Pa)$	3130	3490	3874	4249	4794	3257
$\Delta P_b(Pa)$	3272	3651	4068	4456	5180	3402
$\xi(adim)$	11.0	12.4	14.7	16.9	24.7	11.4

Table 2: Variation of pressure due to the friction forces (ΔP_f) and to the buoyancy forces (ΔP_b). ξ is the corresponding friction factor.

In table 2, we give the actual pressure loss ΔP_f calculated from the numerical integration of the losses inside the IHX (equation 18) and the pressure increase, ΔP_b, due to the driving buoyancy forces, calculated with equation 21. We give also the corresponding friction factor, ξ, calculated with equation 22.

The first five cases have been run for 4000 transient iterations of $0.05\ s$ to get a reasonably converged solution. The sixth case is intermediary between the first and the second case but has been run for 12000 iterations and gives a very good convergence of the monitored values.

We plot the mean temperature profiles along the vertical axis for each case in Figures 7 to 9. These values are calculated by averaging on each plane of cells and taking separately into account all fluid cells which are inside and outside the IHX. All fluid cells located under the IHX are considered inside the IHX.

In figure 10, we plot the temperature through the IHX. This temperature presents a local minimum at the top of the IHX. This is because the IHX top center is a stagnation point for the flow. This stagnation point could be a source of natural instability and create a strong temperature gradient. The flow temperature gets more homogeneous while going downwards.

Figure 11 shows the section integrated velocity module and kinetic energy vertical profiles in the region outside the IHX. It can be seen that the flow stratifies and becomes quasi laminar around the level -6000 (in mm). Conferming that the bypass flowrate is very low.

In figure 12, we show the temperature distribution of the primary coolant through the downcomer channel. In figure 13, we show the temperature field of the primary coolant close to the inner walls and to the outer wall of the downcomer channel. It can be seen from these figures that most isothermal lines are quasi-horizontal conferming a stable thermal stratification.

In figure 14, we show the temperature map for the primary and the secondary coolant at the top of the IHX for case 2. It can be seen that the maximum oil temperature is about $8\ K$ over the mean outlet temperature.

The flow velocity and recirculation patterns can be observed in figures 15, 15 and 17.

While the flow globally passes through the IHX, there are two main recircula-

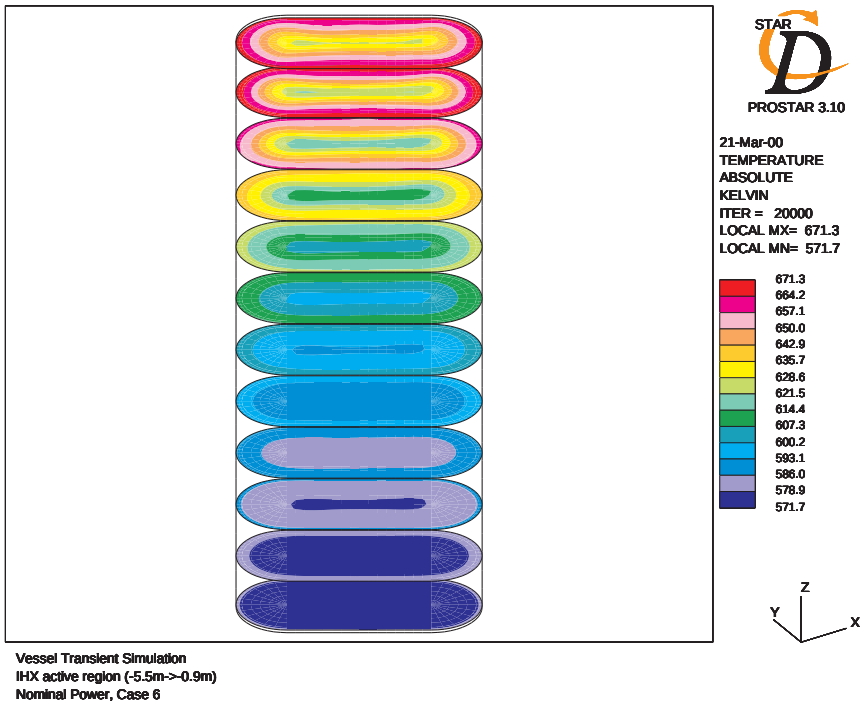

Figure 10: IHX (Pb-Bi part) temperature distribution in case 6.

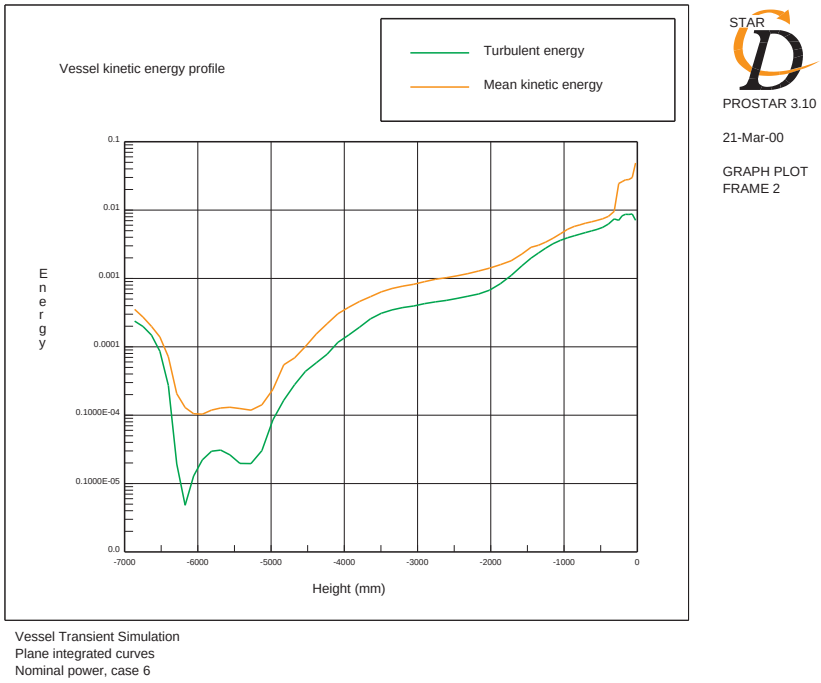

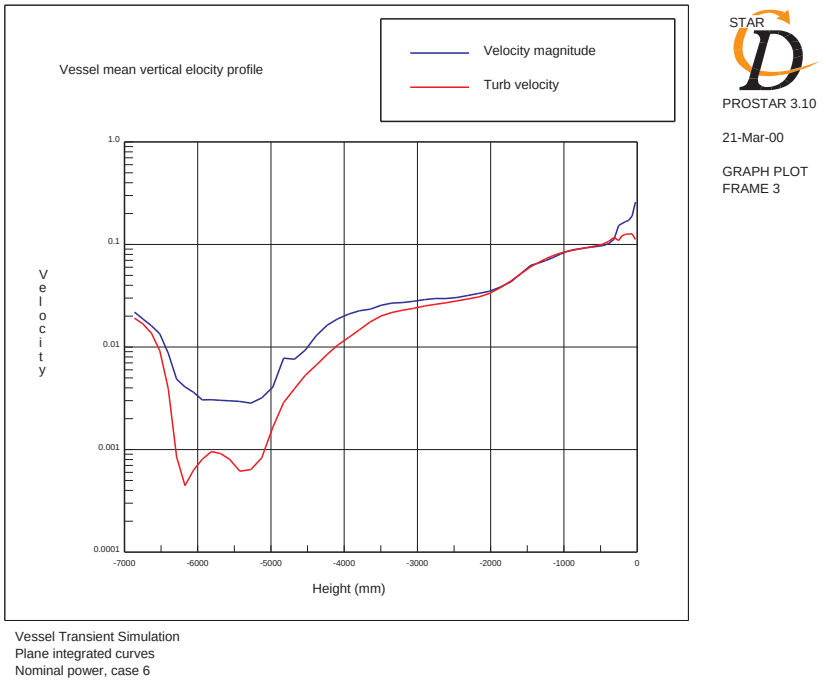

Figure 11: Mean vertical profiles of kinetic energy and velocity module for case 6. Averages are made over an horizontal plane, excluding the IHX.

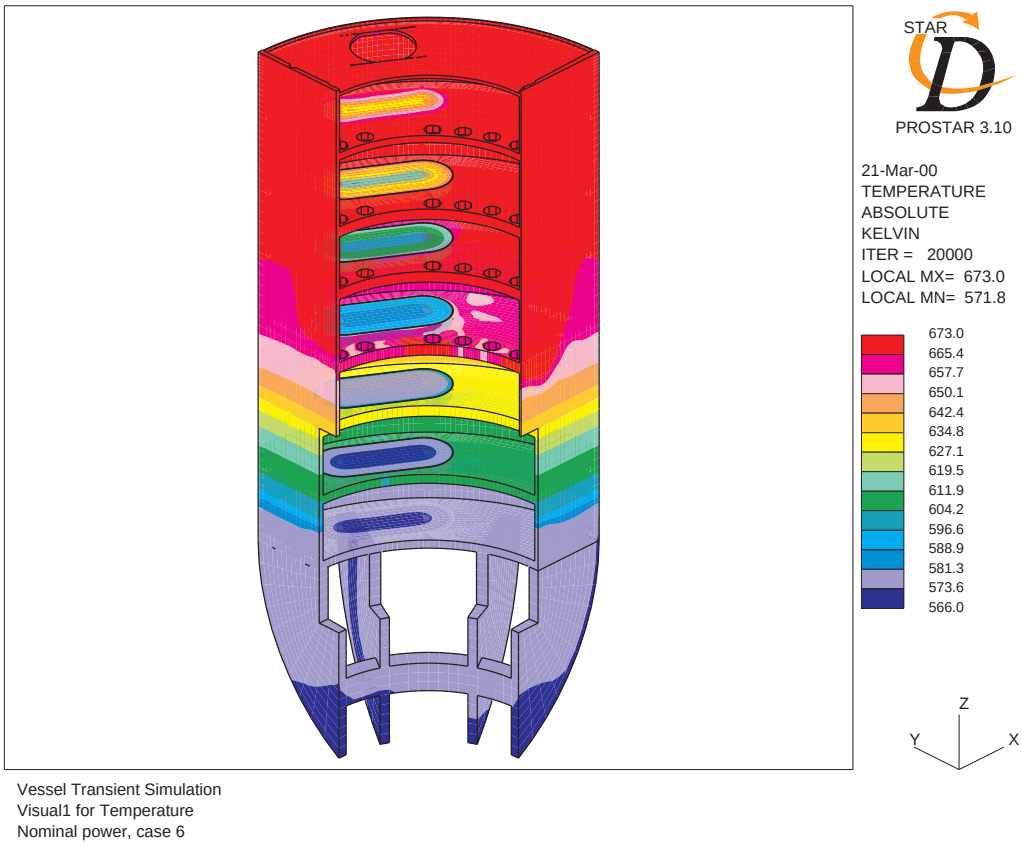

Figure 12: Temperature distribution of the primary coolant throughout the downcomer channel, case 6.

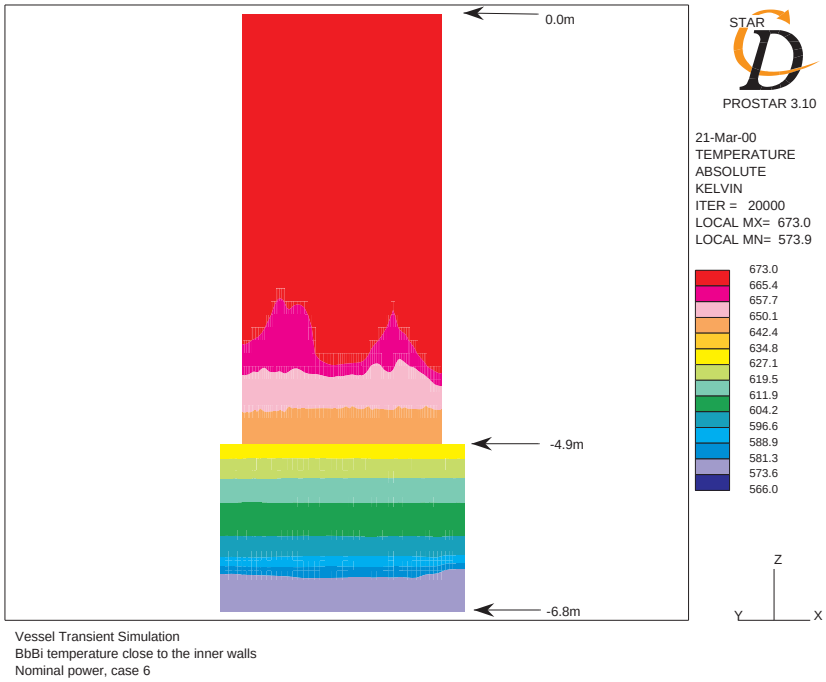

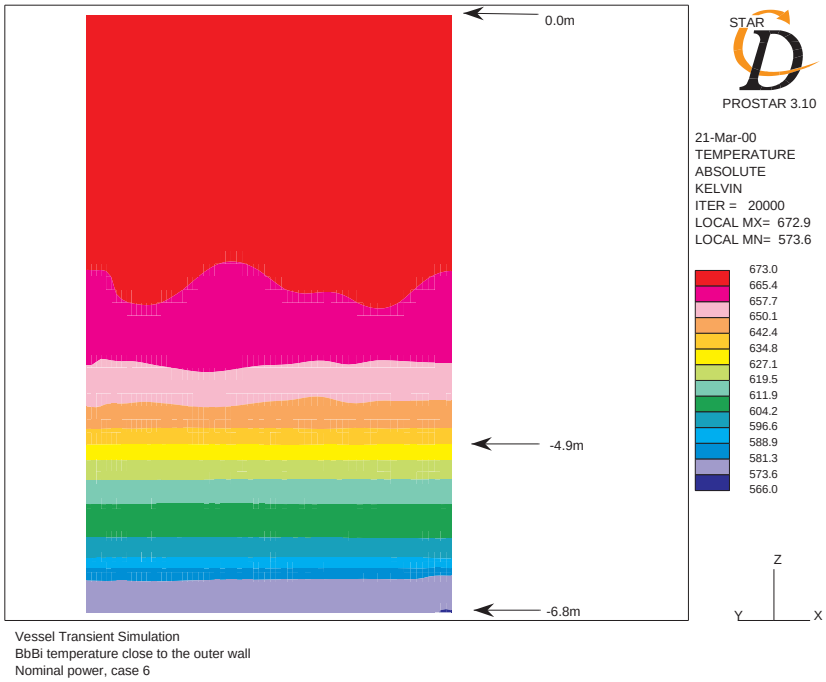

Figure 13: Temperature field of the primary coolant close to the inner walls (up) and to the outer wall (down) of the downcomer channel.

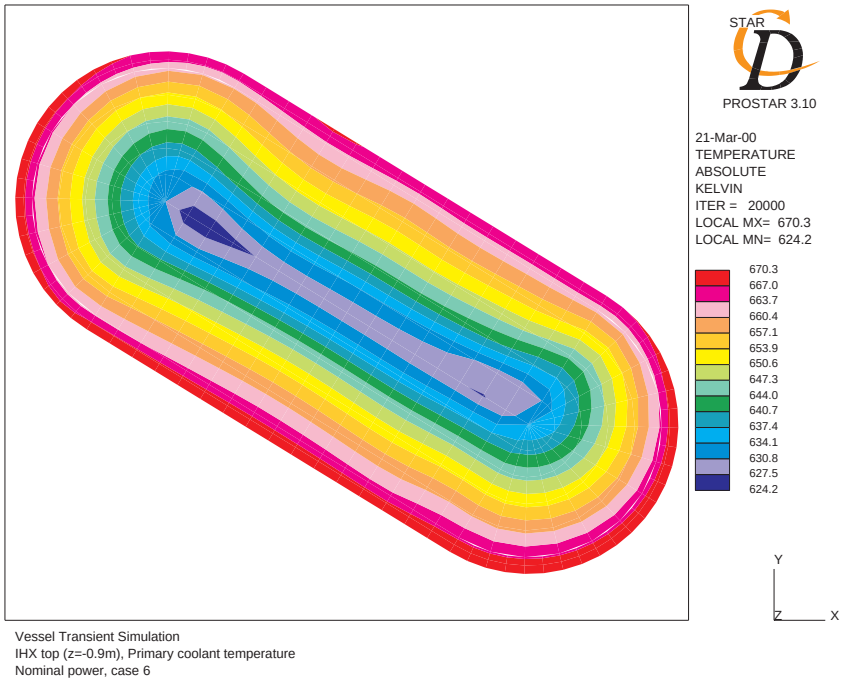

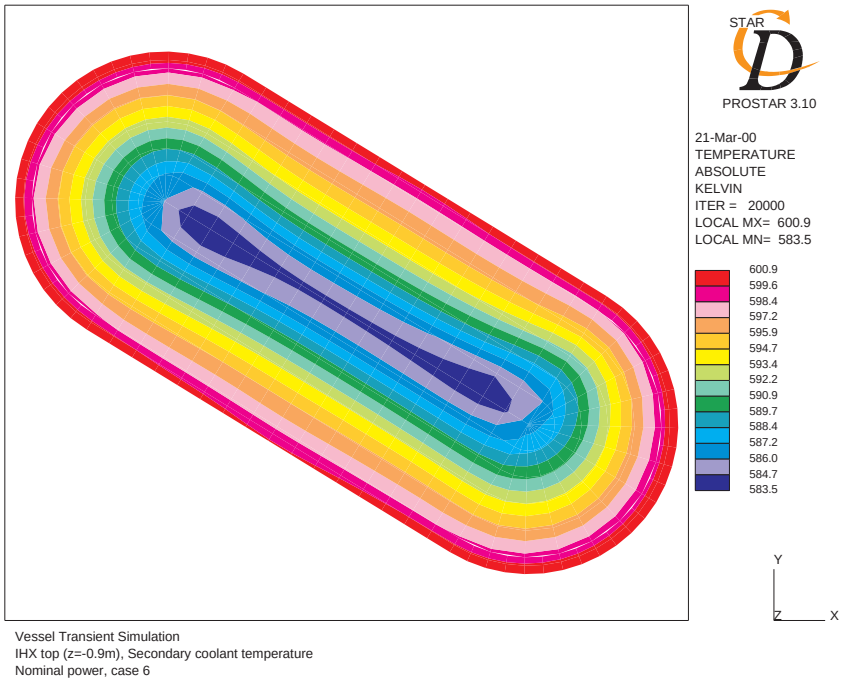

Figure 14: Temperature distribution of the primary coolant (up) and rising secondary coolant (down) at the top of the IHX, case 6.

Mass flow rate (kg/s)	Inside IHX	Outside IHX	bypass fraction
Case 1	1424.5	23.1	1.59 %
Case 2	1418.0	23.5	1.62 %
Case 3	1380.0	70.9	4.89 %
Case 4	1341.6	109.5	7.56 %
Case 5	1151.3	298.1	20.6 %
Case 6	1433.4	14.6	1.01 %

Table 3: Mass flow rate inside and bypassing the IHX for all cases considered.

Heat power (kW/s)	Case 1	Case 2	Case 3	Case 4	Case 5	Case 6
absorbed by the IHX	20,845	20,792	20,475	20,071	18,593	20,896
exchanged between oil fluxes	3,955	3,953	3,862	3,727	3,368	3,995
exchanged through the IHX shell	560.	612.	675.	759.	849.	558.
coming from the tubes	157.4	127.7	102.4	81.4	46.8	156.1
coming from the inner walls	30.0	24.5	19.6	15.3	8.08	29.7
released through the RVACS	66.7	67.9	69.1	70.3	72.5	67.3
released through the IHX top	172.0	171.8	171.5	171.2	170.4	172.0

Table 4: Heat exchanges throughout the computational domain.

tion patterns, one in the upper part with hot fluid and one in the lower part with cold fluid. These two recirculation patterns seem to play an important role in the thermal stratification of the fluid outside the IHX for what concerns the width of the stratification region.

One can see that there is a noticeable downward flow along the tubes which goes down to the stratification region and then turns back to the IHX inlet. When the mass flow rate out of the IHX becomes non-negligible, we can see from the IHX mean temperature curves, figures 8 and 9, that the fluid temperature rises noticeably after leaving the porous region. This is caused by the fact that some hot liquid enters the IHX from the bottom side.

The flow in the outlet of the IHX is very homogeneous and concentrated but is not aligned with the outlet. Then, part of the flow goes laterally up to the symmetry plane and rises up to the stratified zone before slowly converging to the outlet.

The mass flow rates inside and bypassing the IHX for all cases considered are given in table 6.

The list of the heat exchanges throughout the computational domain are given in table 6.

In figure 18, we present the residuals and the monitored cell value history for Case 6 simulation. The simulation is pseudo-transient using 12000 iterations of

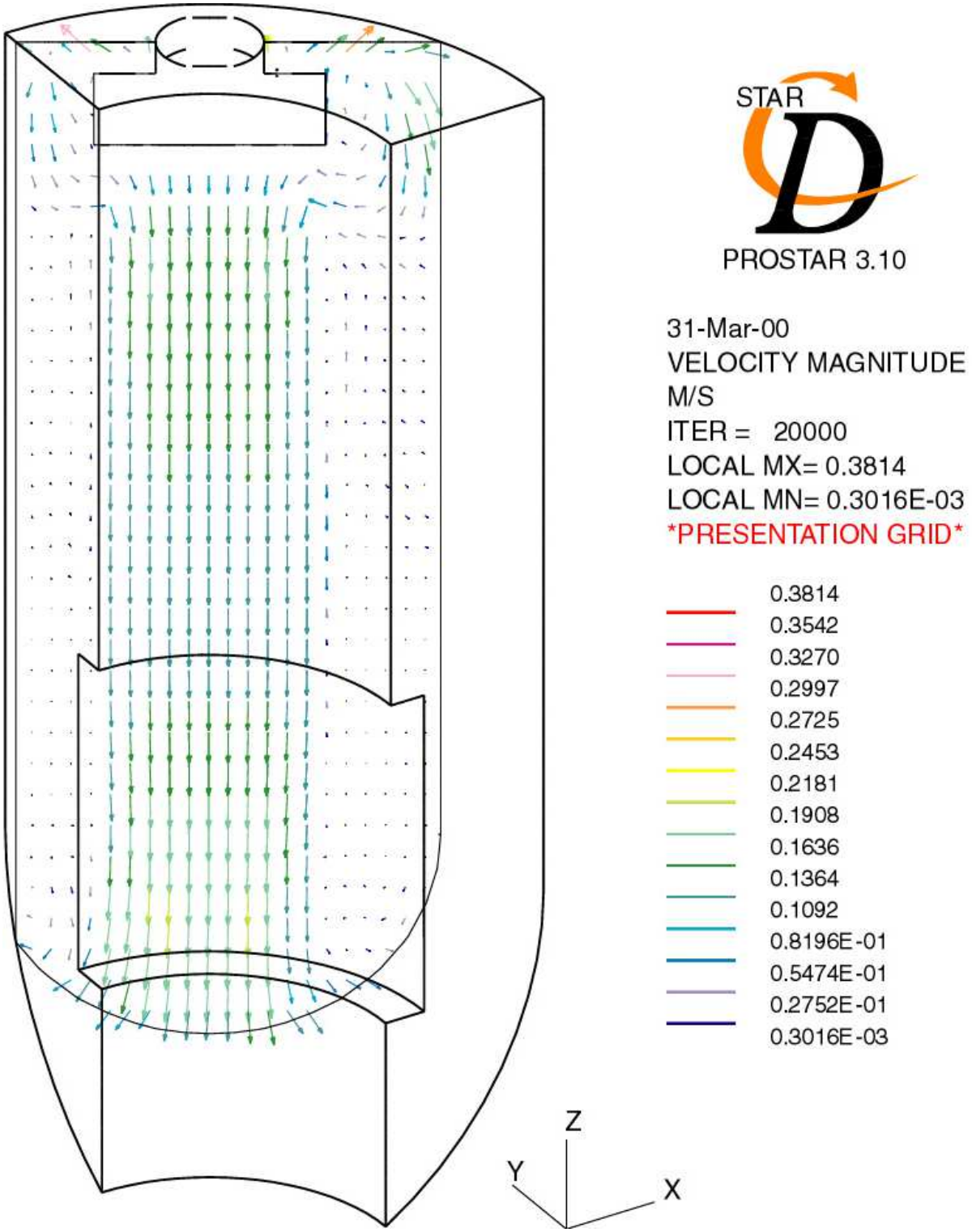

Figure 15: Velocity field over the first vertical symmetry planes of the IHX, case 6

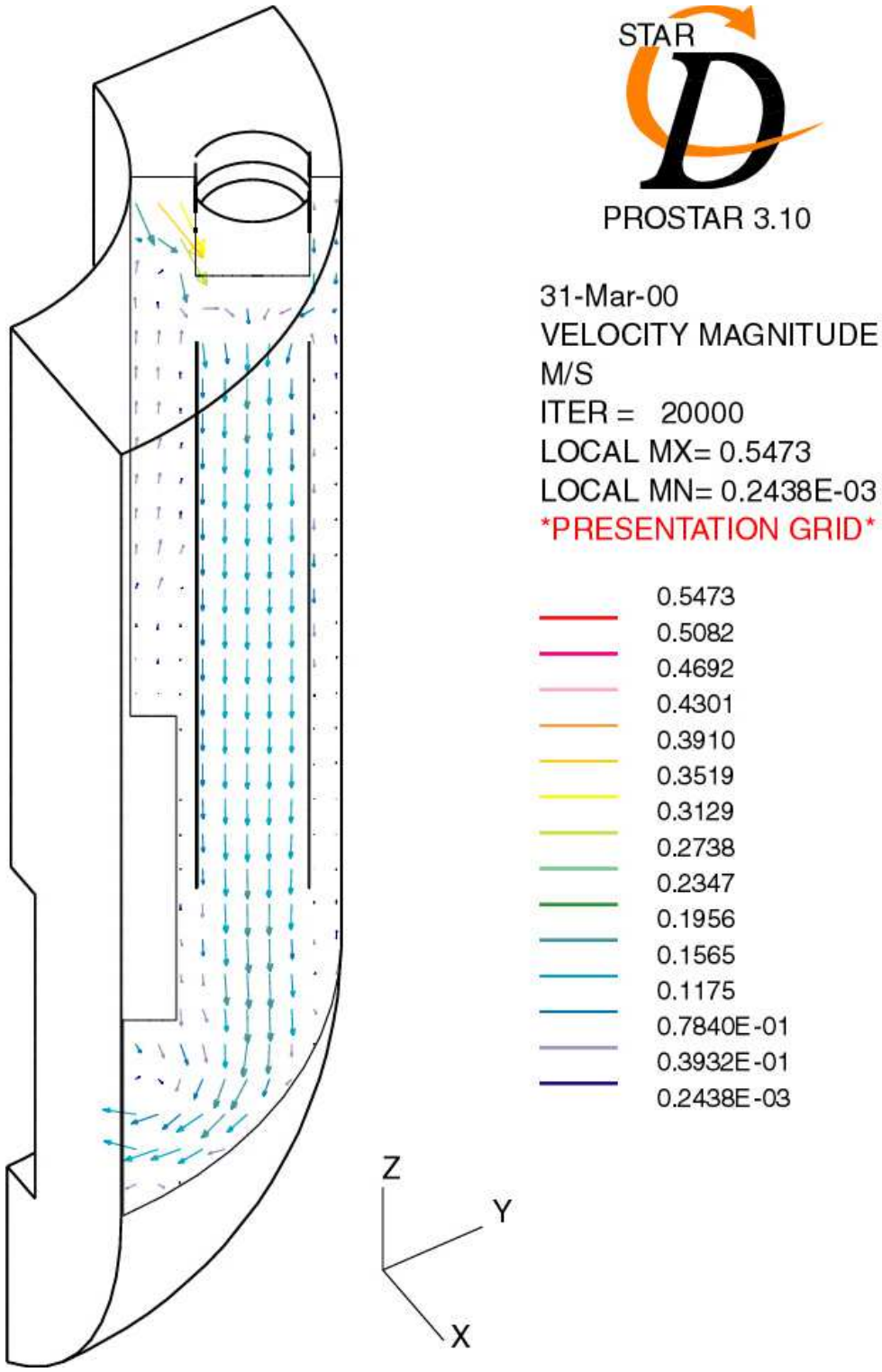

Figure 16: Velocity field over the second vertical symmetry planes of the IHX, case 6

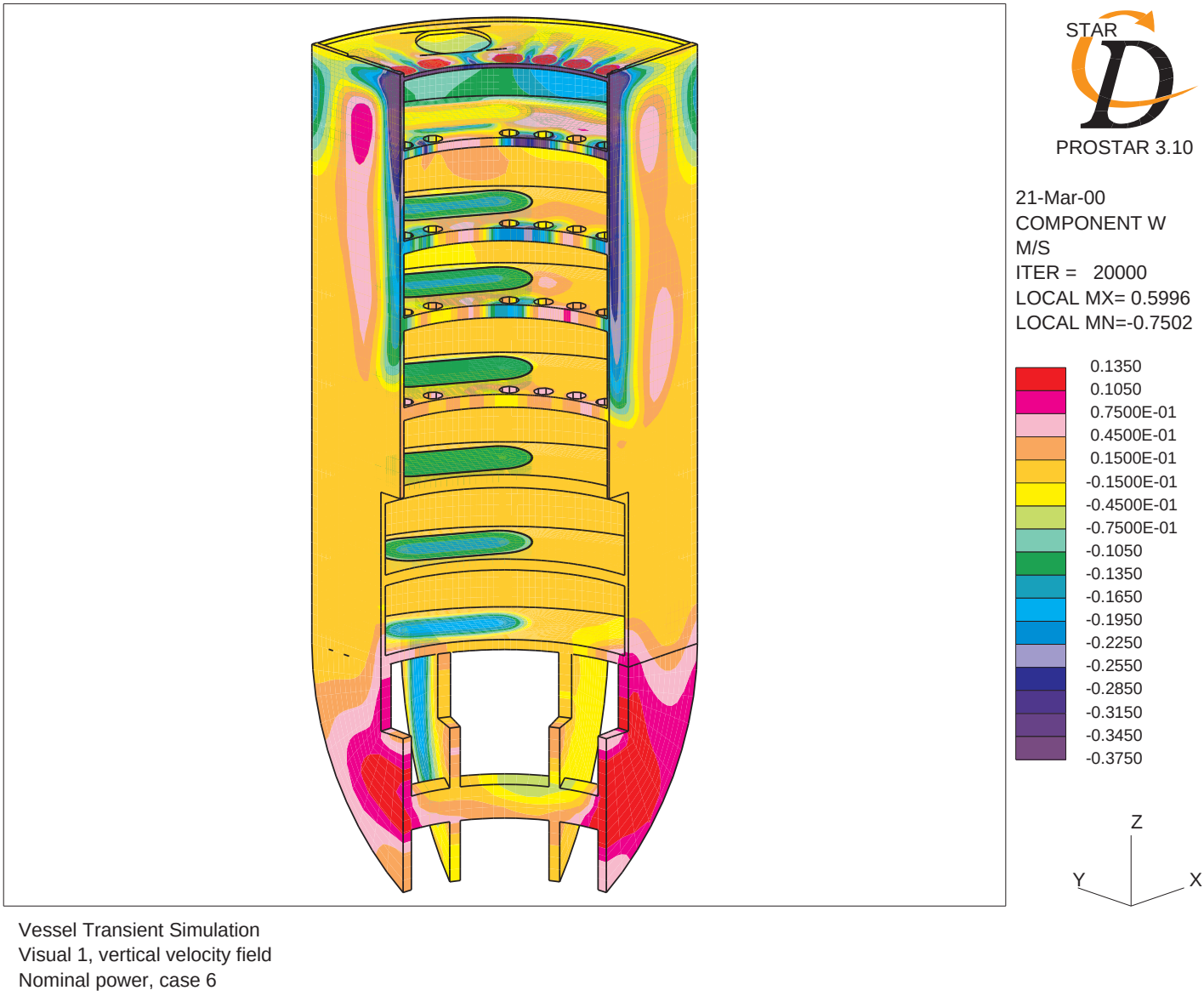

Figure 17: Vertical velocity field throughout the computational domain, case 6.

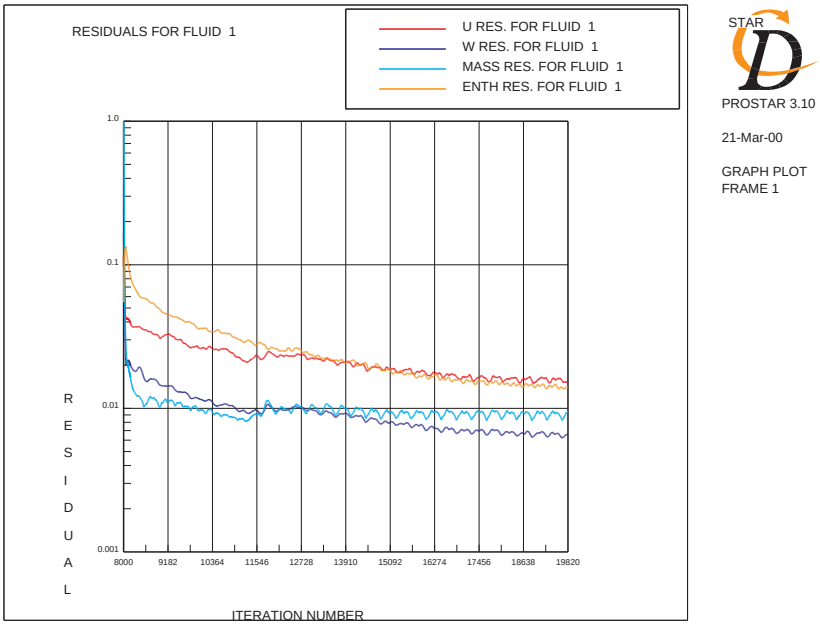

Vessel Transient Simulation
Residual history for PbBi
Nominal power, case 6

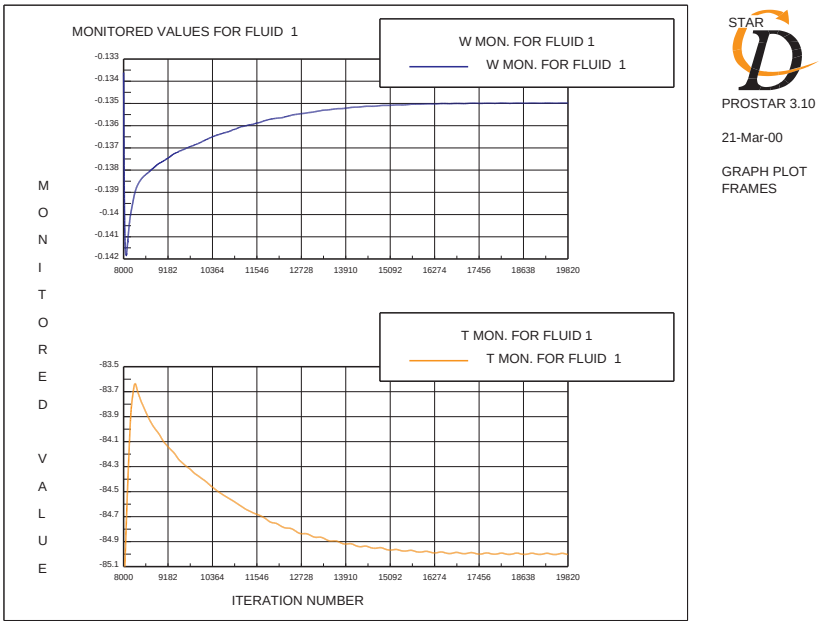

Vessel Transient Simulation
Monitored values for PbBi
Nominal power, case 6

Figure 18: Residual history (up) and monitored value at IHX center (low) for case 6. The temperature curve is relative to the reference temperature $T_{ref} = 400\ ^oC$.

0.05s of the SIMPLE algorithm. It is a restart simulation from the converged simulation of Case 2. So, it also gives insights on the time response for an incidental configuration such as a sudden variation of the IHX resistance. The monitored cell is taken at the center of the IHX, giving an idea of the mass flow rate evolution. We can see that the monitored curves are very regular. The vertical velocity converges very well while the temperature curve shows a very small amplitude ($10^{-2}\ K$) periodic oscillation whose period is about 30 seconds. The residual curves are very regular except for the same small periodic oscillation. The relative convergence may seem very slow, this is because the initial condition is only a small perturbation of the solution.

7 Conclusion

We have successfully performed a 3D simulation of the EADF downcomer channel coupled with the IHX taking into account all relevant heat transfer phenomena. The flow configuration results from the equilibrium between the buoyancy driving forces and the the viscous friction forces in the IHX. The flow outside the IHX is thermaly and dynamically strongly stratified. The width of the stratification is controlled by the inlet and the outlet configuration through secondary flow recirculations. A pressure drop through the IHX is acceptable up to $3500\ Pa$ (case 2) but should not reach $3900\ Pa$ (case 3) to avoid an excessive bypass flow and inflow through the IHX bottom.

References

[1] C. Rubbia et al. Conceptual design of a fast neutron operated high power energy amplifier. Technical Report CERN/AT/95-44(ET), CERN, Geneva, September 29 1995.

[2] Ansaldo; CRS4; ENEA; INFN. Energy amplifier demonstration facility reference configuration. summary report. Technical Report Ansaldo Report EA B0.00 1 200, Ansaldo, Genova, January 1999.

[3] G. Bianchini; M. Carta; A. D'Angelo; F. Norelli. New mathematical models implemented in tieste-minosse code. Technical report, ENEA Divisione Sistemi Energetici Ecosostenibili, 02 2000. DT-SDA-00023.

[4] Corsini. Primary coolant temperature profiles in the downcomer of the adsdf. Technical Report ADS 5 TRLX 0275, ANSALDO, 1999.

[5] L. Maciocco; V. Bellucci; S. Buono; G. Fotia; V. Moreau; M. Mulas; G. Siddi; L. Sorrentino. Design and optimisation of a liquid metal spallation target for the energy amplifier prototype. In *AccApp'98 2nd International Topical*

Meeting on Nuclear Applications of Accelerator Technology, La Grange Park Illinois 60526 USA, Septembre 20-23 1998. American Nuclear Society Inc.

[6] V. Bellucci; S. Buono; G. Fotia; L. Maciocco; V. Moreau; M. Mulas; G. Siddi; L. Sorrentino. Thermalhydraulic design of the fuel element of the energy amplifier prototype. Technical report, CRS4, 1998.

[7] V. Bellucci; S. Buono; L. Maciocco; V. Moreau; L. Sorrentino. Numerical simulation of the energy amplifier demonstration facility vessel. Technical report, CRS4, 1999. Internal Note 99-2.

[8] S. Buono. Minutes of the first meeting of the benchmark working group on heavy liquid metal thermal-hydraulics. CERN Geneva, June 29-30 1999.

[9] Jaffrelot Michel. Dimensionnement et optimisation de l'échangeur de chaleur du prototype de l'amplificateur d'energie. Master's thesis, Ecole des mines d'Albi, 1998.

[10] Computational Dynamics Limited. *Methodology STAR-CD version 3.10*, 1999.

[11] C. Aragonese; S. Buono; L. Maciocco; V. Moreau; L. Sorrentino. A heat exchanger design for the separated window target of the eadf. Technical report, CRS4, 2000. to appear.

[12] Ansaldo. Personal communication.